

Article

## Oxygen Storage Capacity and Oxygen Mobility of Co-Mn-Mg-Al Mixed Oxides and Their Relation in the VOC Oxidation Reaction

María Haidy Castaño, Rafael Molina and Sonia Moreno \*

Estado Sólido y Catálisis Ambiental (ESCA), Departamento de Química, Facultad de Ciencias, Universidad Nacional de Colombia, Cra 30 N° 45-03, Bogotá, Colombia;  
E-Mails: mhcastanor@unal.edu.co (M.H.C.); ramolinag@unal.edu.co (R.M.)

\* Author to whom correspondence should be addressed; E-Mail: smorenog@unal.edu.co;  
Tel.: +571-3165000 (ext. 14473); Fax: +571-3165220.

Academic Editor: Jean-François Lamonier

Received: 26 February 2015 / Accepted: 22 May 2015 / Published: 29 May 2015

---

**Abstract:** Co-Mn-Mg-Al oxides were synthesized using auto-combustion and co-precipitation techniques. Constant ratios were maintained with  $(\text{Co} + \text{Mn} + \text{Mg})/\text{Al}$  equal to 3.0,  $(\text{Co} + \text{Mn})/\text{Mg}$  equal to 1.0 and  $\text{Co}/\text{Mn}$  equal to 0.5. The chemical and structural composition, redox properties, oxygen storage capacity and oxygen mobility were analyzed using X-ray fluorescence (XRF), X-ray diffraction (XRD), Raman spectroscopy, scanning electron microscopy (SEM), temperature-programmed reduction of hydrogen ( $\text{H}_2$ -TPR), oxygen storage capacity (OSC), oxygen storage complete capacity (OSCC) and isotopic exchange, respectively. The catalytic behavior of the oxides was evaluated in the total oxidation of a mixture of 250 ppm toluene and 250 ppm 2-propanol. The synthesis methodology affected the crystallite size, redox properties, OSC and oxide oxygen mobility, which determined the catalytic behavior. The co-precipitation method got the most active oxide in the oxidation of the volatile organic compound (VOC) mixture because of the improved mobility of oxygen and ability to favor redox processes in the material structure.

**Keywords:** co-precipitation; hydrotalcite; auto-combustion; oxygen mobility; isotopic exchange; oxygen storage

---

## 1. Introduction

A number of studies have investigated the individual oxidation of volatile organic compounds (VOCs), such as toluene, ethyl acetate, 2-propanol, among others [1–4]. However, in practical applications, emissions from industrial sources or mobile sources contain VOC mixtures with different compositions and concentrations, which increases the difficulty of predicting catalytic behavior; thus, new catalytic materials must be developed that can achieve a greater efficiency in removing mixtures of these contaminants.

According to certain authors, the oxidation of a mixture provokes the inhibition of the reaction, which is manifested as an increase in the temperature required for the conversion of a compound. This behavior could occur as a result of competition among VOCs for adsorption at the active sites [5,6] or competition by oxygen atoms chemisorbed [7].

According to the literature [8,9], the behavior of components in a mixture has been difficult to predict because such behavior is dependent on the composition of the mixture, number and proportion of components, and nature of the catalyst

Mixed Mn and Co oxides are considered valuable materials in oxidation reactions because of their ability to occur in multiple oxidation states and optimum oxygen storage capacity [10]. In general, a redox mechanism occurs in the oxidation of volatile organic compounds in which the surface oxygen or lattice oxygen in the oxide may be involved. In Co and Mn oxides, the lattice oxygen has been found to participate in the oxidation of propene, CO, and VOCs [11–13] demonstrating an elevated oxygen mobility in these materials.

Numerous synthesis methods have been used to prepare metal oxides [14,15] and co-precipitation is one of the most frequently used for the generation of hydrotalcites as precursors of mixed oxides [16,17]. The thermal decomposition of hydrotalcites leads to the formation of oxides with interesting properties, such as elevated surface area (100–300 m<sup>2</sup>/g), homogeneous element interdispersion, active phase dispersion, synergistic effects and basic characteristics [17,18]. Similarly, auto-combustion represents another important synthesis method in the preparation of mixed oxides in shorter synthesis times and without a precursor requirement. The characteristics that contribute to the unique properties of synthesized products can be summarized as follows: (i) initial reaction medium (aqueous solution) can mix reactants at a molecular level; (ii) high reaction temperatures ensure high purity and crystallinity products; and (iii) short process duration and gas formation inhibit increases of particle size and favor the synthesis of solids with large surface area [19–21].

Studies on mixed oxides obtained by the use of hydrotalcite-type precursors and prepared by the auto-combustion method that focus on their oxygen storage ability, reoxidation capacity, oxygen mobility and relationship between these properties and their catalytic performance are limited in number. In the present work, relationships between the catalytic activity in the oxidation of a VOC mixture and oxygen mobility and oxygen storage capacity in the Co-Mn mixed oxides are established.

## 2. Results and Discussion

### 2.1. Precursors Characterization

The diffraction patterns of the Mn and Co samples obtained by the auto-combustion and co-precipitation methodologies prior to the calcination process at 500 °C are presented in Figure 1. In the material prepared by co-precipitation, the typical formation of the hydrotalcite-type precursor (HTCoMn) is observed, with intense signals at 11.3, 22.6 and 34.4° 2 $\theta$ , which indicate the generation of a well-crystallized layered structure with 3R symmetry [22]. In addition to the hydrotalcite phase, signals attributed to the MnCO<sub>3</sub> rhodochrosite phase and the Mn<sub>3</sub>O<sub>4</sub> hausmannite phase (JCPDS 44-1472 and JCPDS 24-0734) are observed. The formation of the MnCO<sub>3</sub> phase in the HTCoMn sample is consistent with that reported for Mn hydrotalcites; however, the presence of Co most likely contributes to the greater generation of this phase because Co<sup>2+</sup> can be incorporated more efficiently into the layered structure as a result of similarities in the ionic radii of Co<sup>2+</sup> and Mg<sup>2+</sup> (0.65 Å and 0.72 Å, respectively) compared with that of Mn<sup>2+</sup> (0.83 Å), increasing the presence of Mn<sup>2+</sup> surface species capable of reacting with the carbonates and producing more MnCO<sub>3</sub> [23,24].

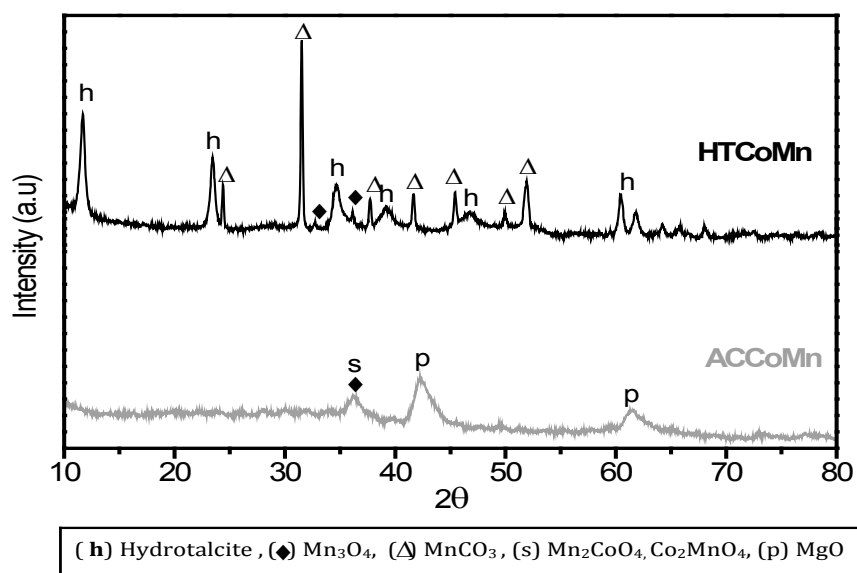


**Figure 1.** Diffraction patterns of the samples before the calcination process at 500 °C.

The lattice parameters  $a$  and  $c$  (distance between two neighboring cations and thickness of three brucite layers along with their interlayer space, respectively) calculated for HTCoMn correspond to 0.306 nm and 2.27 nm, respectively. The similarity between the values calculated for HTCoMn and values reported in the literature ( $a = 0.306$  nm and  $c = 2.34$  nm) confirm the formation of a layered structure [25]. However, the decrease in value of parameter  $c$  in HTCoMn is most likely because of an increment of the electrostatic forces between the layers and interlayer of the structure, an effect that is only possible if ions such as Mn<sup>3+</sup> are present in the brucite layers.

On the other hand, the X-ray diffraction (XRD) profile of the sample obtained by auto-combustion exhibits direct formation of the mixed oxide. The peaks at 42.4 and 61.7° 2 $\theta$  are attributed to the MgO periclase phase (JCPDS 45-0946), whereas the signal at 36.2° 2 $\theta$  is attributed to the formation of Mn or

Co spinels. The lattice parameter  $a$  calculated for the oxide using the  $d_{(200)}$  reflection of the periclase phase corresponds to 0.427 nm. This value is higher than that found for the Mg-Al oxide synthesized by auto-combustion (0.419 nm) suggesting the partial incorporation of Co and/or Mn ions into the MgO-Al<sub>2</sub>O<sub>3</sub> oxide matrix.

## 2.2. Characterization of the Mixed Oxides

### 2.2.1. Chemical and Structural Composition

In hydrotalcites to maintain the ratio  $M^{2+}/M^{3+} = 3.0$  or  $M^{3+}/(M^{2+} + M^{3+}) = 0.25$  is of great importance because it can form a layered structure that is characteristic of layered double hydroxides without the presence of undesired species, such as Al(OH)<sub>3</sub> or Mg(OH)<sub>2</sub> [18].

The elemental chemical analysis of the Co-Mn mixed oxides is indicated in Table 1. The results reveal that the molar ratios of the mixed oxides synthesized by both methodologies present values similar to the nominal values for  $(Mn^{2+} + Co^{2+} + Mg^{2+})/Al^{3+} \cong 3.0$ ,  $(Co^{2+} + Mn^{2+})/Mg^{2+} \cong 1.0$  and  $Co^{2+}/Mn^{2+} \cong 0.5$ .

**Table 1.** Chemical composition of the mixed oxides and particle size (Dp).

Sample	$(Mn^{2+} + Co^{2+} + Mg^{2+})/Al^{3+}$	$(Mn^{2+} + Co^{2+})/Mg^{2+}$	$Co^{2+}/Mn^{2+}$	Dp (nm) ± 3nm
ACCoMn	3.3	1.6	0.5	7
CPCoMn	2.9	1.4	0.6	20

On the other hand, it is widely reported in the literature that the thermal decomposition of Mg-Al hydrotalcites starts with the loss of interlayer water molecules at 150–200 °C, followed by the collapse of the hydroxide layers in the temperature range of 300–400 °C and the total loss of the layered structure above 500 °C [26]. Figure 2 shows the diffraction patterns of the Co-Mn mixed oxides obtained by auto-combustion (ACCoMn) and generated after the thermal decomposition of the hydrotalcite-type precursor at 500 °C (CPCoMn). The CPCoMn profile does not show signals associated with the hydrotalcite phase, confirming the total destruction of the layered structure and formation of the corresponding mixed oxide.

After the calcination process, more spinel-type species are segregated in the ACCoMn because of the oxidation of Mn and Co ions after the thermal process. These species can be derived from the Co-Mn-Mg-Al mixed oxide matrix as indicated by the increased signal intensity at  $\sim 36^\circ 2\theta$  and decreased signal intensity corresponding to the MgO phase, which shifts towards higher  $2\theta$  values ( $\sim 44^\circ$ ) with respect to the non-calcined ACCoMn oxide (Figure 1).

The diffraction profiles of ACCoMn and CPCoMn exhibit signals that may correspond to the Mn<sub>3</sub>O<sub>4</sub>, Mn<sub>2</sub>MgO<sub>4</sub>, Mg<sub>2</sub>MnO<sub>4</sub>, MnAl<sub>2</sub>O<sub>4</sub>, Co<sub>3</sub>O<sub>4</sub>, CoAl<sub>2</sub>O<sub>4</sub> and Co<sub>2</sub>AlO<sub>4</sub> phases (JCPDS 24-0734, JCPDS 23-0392, JCPDS 19-0773, JCPDS 29-0880, JCPDS 042-1467, JCPDS 044-0160 and JCPDS 030-0814, respectively) or mixed oxides of the type Mn<sub>3-x</sub>Co<sub>x</sub>O<sub>4</sub> ( $x = 1, 2$ ), whose maxima are similar and their exact assignment is unknown. Furthermore, these oxides show the formation of an MgO phase with peaks that correspond to the signals at  $\sim 42.9$  and  $\sim 63.7^\circ 2\theta$ .

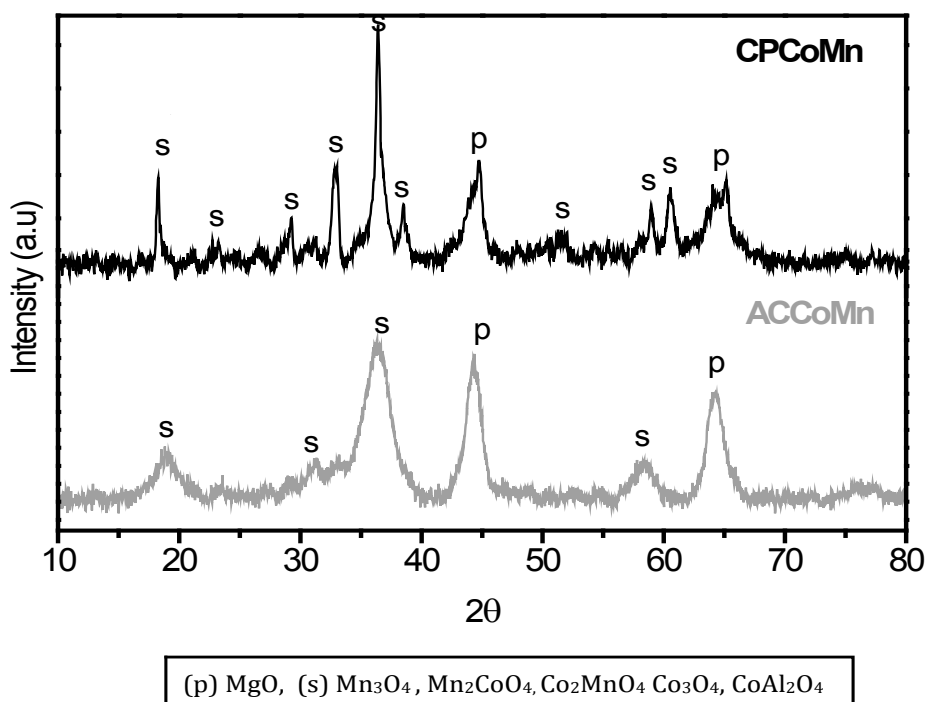


**Figure 2.** Diffraction patterns of the mixed oxides synthesized by co-precipitation and auto-combustion.

The presence of Mn<sub>3</sub>O<sub>4</sub> and Co<sub>3</sub>O<sub>4</sub> in the ACCoMn and CPCoMn oxides coincide with results reported in the literature, which indicate that when Co and Mn are present in solution, the simultaneous precipitation of Co<sub>3</sub>O<sub>4</sub> and Mn<sub>3</sub>O<sub>4</sub> can occur [27]. Furthermore, the formation of a solid solution of Mn<sub>3-x</sub>Co<sub>x</sub>O<sub>4</sub> (for  $x = 0-3$ ) can be conducted because of the similarity of ionic radii between Co<sup>2+</sup> (0.65 Å) and Co<sup>3+</sup> (0.55 Å) ions and Mn<sup>2+</sup> (0.83 Å) and Mn<sup>3+</sup> (0.58 Å) ions; thus, a dissolution of Co ions can occur in the Mn oxide lattice to form solid solutions [23]. This result was reported by Sinha *et al.* [28] who indicated that Co<sup>2+</sup> can randomly substitute Mn<sup>2+</sup> or Mn<sup>3+</sup> at tetrahedral or octahedral sites, respectively, because of its affinity towards both sites.

The average size of the crystalline aggregate of the ACCoMn and CPCoMn mixed oxides was calculated using the Scherrer equation and hausmannite (211) plane (Table 1), and this value correspond to the mixture of different spinel-type species.

The ACCoMn solid exhibits a much smaller particle size than that obtained by co-precipitation, which is attributed to the great amount of gaseous products formed during synthesis that avoid interparticle contact and improve dispersion in terms of the crystallite size. The greater crystallite size of CPCoMn is justified because of the aging processes that occur during synthesis by co-precipitation, which favors crystal growth.

The N<sub>2</sub> adsorption-desorption isotherms of the Co-Mn mixed oxides are shown in Figure 3. CPCoMn reveals a type II isotherm characteristic of macroporous materials with an H1 hysteresis loop, associated with a uniform pore arrangement. On the other hand, ACCoMn exhibits a type IV isotherm characteristic of mesoporous materials with a type H3 hysteresis loop proper of pores in a slit form [29].

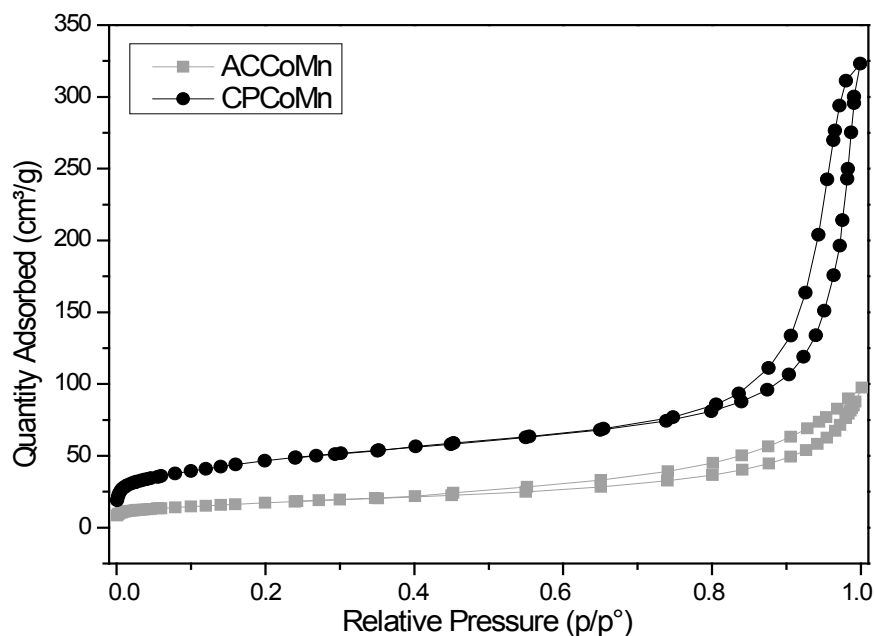


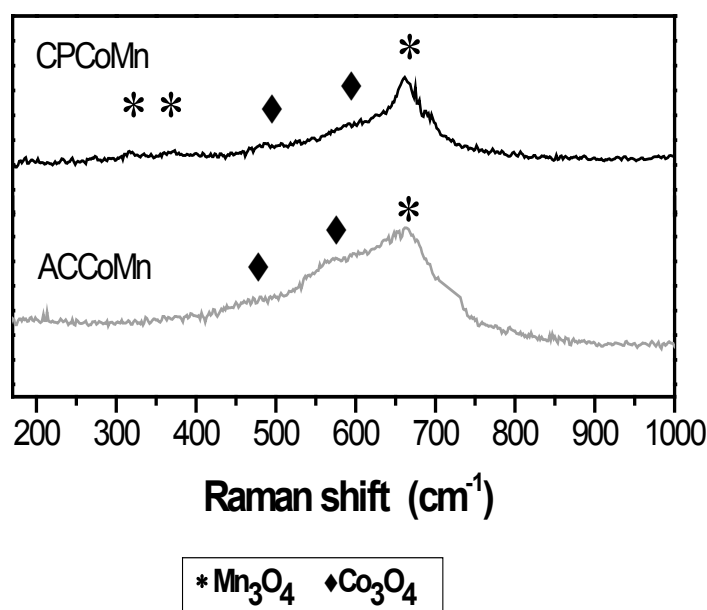
**Figure 3.** Nitrogen adsorption–desorption isotherms of the Co-Mn oxides.

The BET specific areas for CPCoMn and ACCoMn correspond to  $161 \text{ m}^2/\text{g}$  and  $61 \text{ m}^2/\text{g}$ , respectively. The area of the oxide synthesized by co-precipitation is attributed to the formation of pores resulting from the destruction of the lamellar spaces of the hydrotalcite by calcination process (loss of water and carbonates) whereas in the oxide prepared by auto-combustion, the area is the result of the evolution of gases such as  $\text{CO}_2$  and  $\text{H}_2\text{O}$  generated during the combustion process. However, the specific area determined in the ACCoMn oxide corresponds to an approximation of the real area of the solid due to the presence of pores of a large size (micrometer order) which limit the determination of the textural properties by means of the adsorption of  $\text{N}_2$  technique [30].

Within Mn oxides, the hausmannite phase ( $\text{Mn}_3\text{O}_4$ ) is the most sensitive in Raman spectroscopy, and it has a characteristic intense peak at approximately  $654 \text{ cm}^{-1}$  ( $A_{1g}$ ) that corresponds to the Mn-O vibration of  $\text{Mn}^{2+}$  in a tetrahedral configuration, a weak signal at  $485 \text{ cm}^{-1}$  and two signals with medium intensity at approximately  $310 \text{ cm}^{-1}$  ( $E_g$ ) and  $360 \text{ cm}^{-1}$  ( $T_{2g}$ ). [31].

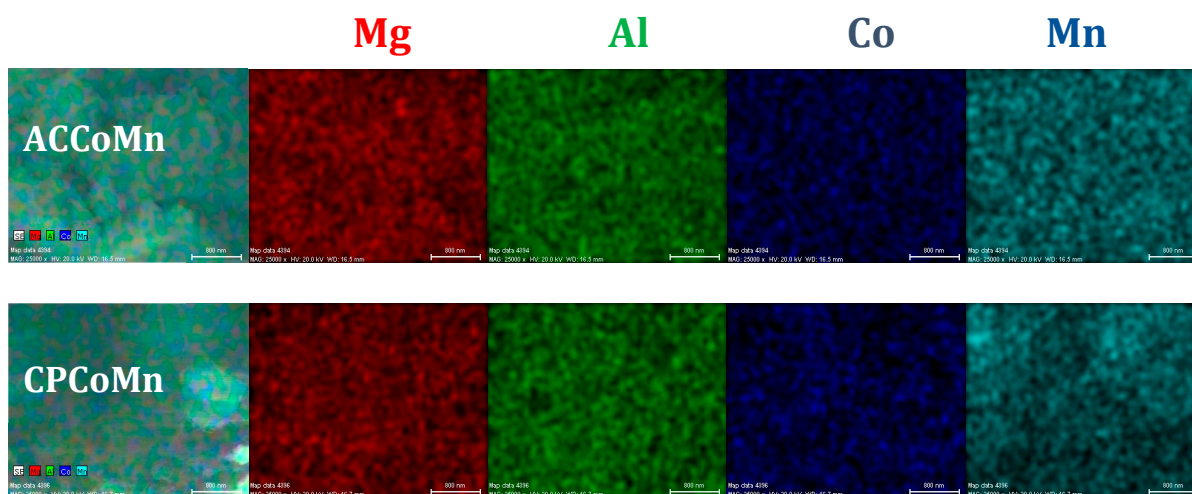
Oxide  $\text{Co}_3\text{O}_4$  has a cubic structure, with the ions  $\text{Co}^{2+}$  and  $\text{Co}^{3+}$  located in the tetrahedral and octahedral positions, respectively, and it presents five Raman-active modes ( $A_{1g}$ ,  $E_g$  and  $3F_{2g}$ ) [32]. One band attributed to octahedral sites ( $\text{CoO}_6$ ) at approximately  $680 \text{ cm}^{-1}$ , three bands with medium intensity at  $480 \text{ cm}^{-1}$ ,  $530 \text{ cm}^{-1}$  and  $580 \text{ cm}^{-1}$ , and one band characteristic of tetrahedral sites ( $\text{CoO}_4$ ) at  $190 \text{ cm}^{-1}$ .

Figure 4 shows the Raman spectra of the mixed oxides prepared by auto-combustion and co-precipitation. It is important to note that the vibrational modes are only associated with the Co-Mn oxides because the modes corresponding to  $\text{MgO}$  and  $\text{Al}_2\text{O}_3$  are not present within the studied range [33,34].



**Figure 4.** Raman spectra of the Co-Mn mixed oxides.

The CPCoMn oxide exhibits an intense signal at  $660\text{ cm}^{-1}$  and signals at  $315\text{ cm}^{-1}$  and  $370\text{ cm}^{-1}$ , which are attributed to the presence of the  $\text{Mn}_3\text{O}_4$  phase, along with  $\text{Co}_3\text{O}_4$  signals. The ACCoMn oxide exhibits a signal at  $665\text{ cm}^{-1}$ , which is characteristic of the hausmannite phase, along with  $\text{Co}_3\text{O}_4$  signals. In the spectra of these two solids, a shift towards higher wavelengths is observed in the peak associated with the  $\text{Mn}_3\text{O}_4$  phase, which can be attributed to the incorporation of Co ions into the structure of the  $\text{Mn}_3\text{O}_4$  phase. However, according to the results found for these oxides, the co-existence of individual  $\text{Mn}_3\text{O}_4$  and  $\text{Co}_3\text{O}_4$  phases cannot be ignored. These results verify the predominant formation of the  $\text{Mn}_3\text{O}_4$  phase in the mixed oxides obtained by the two methodologies, which is consistent with XRD results.



**Figure 5.** Chemical mapping performed by EDX for the mixed oxides.

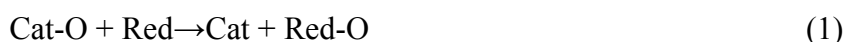
The chemical mapping technique with energy-dispersive X-ray spectroscopy (EDX) was used to study the chemical composition distribution in the mixed oxides in specific regions of the materials, which is presented in Figure 5.

A homogeneous distribution of elements is observed in both solids, indicating that equivalent oxides are obtained by using the auto-combustion and co-precipitation methodologies.

### 2.2.2. Redox Properties and Oxygen Mobility

Taking into account the Mars Van Krevelen mechanism [35] which is commonly accepted in oxidation reactions with metal oxides, a catalyst with a redox pair and high oxygen mobility is required to ensure the reoxidation of the reduced catalyst.

The redox process of the mixed oxides can be described according to the following general mechanism:



The catalyst (Cat-O) is reduced by the substrate (reducer) and then reoxidized by an oxidizer (Ox-O) to its initial state. The net results indicate an oxygen transfer from one species to another, which is verified in the specific reaction of VOCs by the oxidation of the organic compound, reduction of the oxide surface by the loss of surface oxygen atoms, and the subsequent reoxidation of the catalyst [36].

In the present work, the temperature-programmed reduction of hydrogen (H<sub>2</sub>-TPR), oxygen storage capacity (OSC), and oxygen storage complete capacity (OSCC) techniques were used to evaluate the amount and mobility of available oxygen in the materials, and these methods provide complementary information on the redox properties of the oxides.

The H<sub>2</sub>-TPR is appropriate to investigate the amount of active oxygen species and the steps involved in the reduction process of oxides [37]. For Co oxides derived from hydrotalcite precursors, the reduction processes occur at low temperatures (<500 °C) and high temperatures (>700 °C) [38]. The reduction at  $T < 500$  °C is attributed to the reduction of Co oxide to Co metal,  $\text{Co}_3\text{O}_4 \rightarrow \text{CoO} \rightarrow \text{Co}$ , and reduction processes at high temperatures are associated with the presence of Co-Al-type or species with strong interactions within the solid solution [39,40].

The H<sub>2</sub>-TPR profiles of Mn oxides are complex because of the multiple oxidation states of Mn and different chemical environments in which it can be found. However, these profiles can be classified into three main regions: low temperature <300 °C; intermediate temperature 300–550 °C; and high temperatures >550 °C. The reduction processes of MnO<sub>x</sub> species with diverse particle sizes as well as that of Mn<sub>5</sub>O<sub>8</sub> species are assigned to the low temperature region; the transitions of MnO<sub>2</sub>/Mn<sub>2</sub>O<sub>3</sub> to Mn<sub>3</sub>O<sub>4</sub> and Mn<sub>3</sub>O<sub>4</sub> species to the reduced form of Mn (MnO) are assigned to the intermediate region [41,42] and reduction processes of the Mn spinel phases, such as MnAl<sub>2</sub>O<sub>4</sub>, and Mn species that present strong interactions in solid solution are assigned to the high temperature region [43].

Figure 6 shows the H<sub>2</sub>-TPR profiles of the Co-Mn-Mg-Al mixed oxides. The ACCoMn and CPCoMn solids show reduction signals along all of the evaluated temperature ranges. In general, the signals observed for these oxides at temperatures <500 °C are assigned to the reduction of Mn<sup>4+</sup>/Mn<sup>3+</sup>/Mn<sup>2+</sup> species to MnO and Co<sup>3+</sup>/Co<sup>2+</sup> to CoO, whereas the signals observed at temperatures >500 °C are assigned to reduction events of the Co or Mn spinels with Al [27]. The presence of a signal at 895 °C is

indicative of the formation of other species in addition to the  $\text{Mn}_3\text{O}_4$ ,  $\text{Co}_3\text{O}_4$  and  $\text{Mn}_{3-x}\text{Co}_x\text{O}_4$  phases found by XRD for these solids (cobalt aluminates).

The signal at 680 °C in the ACCoMn solid indicates the presence of Mn species with significant interactions in the solid solution or  $\text{MnAl}_2\text{O}_4$ -type spinels that are generated because of the high temperatures that can be reached in the auto-combustion process (1400–1600 °C) [44], which decreases the oxygen mobility inside the material. This signal is not present in the CPCoMn oxide.

According to the XRD and Raman results, the predominant phase in the ACCoMn and CPCoMn oxides corresponds to the  $\text{Mn}_3\text{O}_4$  phase, which is reduced to MnO at approximately 490 °C [24]. Figure 6 shows that this reduction process occurs at 480 and 450 °C for ACCoMn and CPCoMn, respectively, indicating that a lower temperature is required to carry out the  $\text{Mn}_3\text{O}_4$  reduction in the solid synthesized by co-precipitation (CPCoMn). According to certain reports [4,30] this behavior reveals that in the Co-Mn mixed oxides obtained by co-precipitation, the reduction temperatures decrease because of a possible substitution of Co ions by Mn ions in the structure, which leads to a distortion of the lattice and generation of oxygen vacancies that destabilize the Mn-O bond.

In the case of the ACCoMn oxide, the elevated synthesis temperatures favor fusion and coalescence processes in the metals [44], provoking the formation of species with strong interactions that decrease their mobility. Thus, the presence of oxygen vacancies is the determining factor for oxygen mobility, and such mobility increases when the strength of the M-O bond decreases.

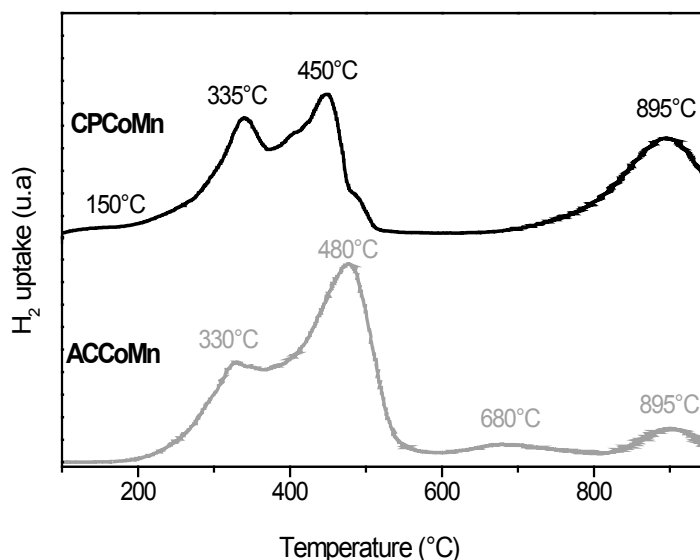


**Figure 6.** Reduction profiles of the Co-Mn mixed oxides.

The quantity of hydrogen consumed by means of the area below the curve permits the estimation of the quantity of species reducible with the temperature. For CPCoMn a  $\text{H}_2$  consumption of  $1257 \mu\text{mol g}^{-1}$  at  $T < 350$  °C was observed which corresponds to the range where the catalytic oxidation of VOCs occurs. For ACCoMn the consumption was  $965 \mu\text{mol g}^{-1}$  in this temperature region. These  $\text{H}_2$  values correspond to 25% and 18% of the total quantity of  $\text{H}_2$  consumed for CPCoMn and ACCoMn, respectively, which indicates that the oxide CPCoMn presents the greatest quantity of reducible species within the temperature range evaluated.

Additionally, the reduction of the CPCoMn oxide begins at lower temperatures, with a peak around 150 °C attributed to the presence of very active species on the surface of this oxide, capable of participating in the catalytic process. This peak is absent in the ACCoMn oxide.

On the other hand, the OSC and OSCC techniques are used to complement the study of surface and bulk oxygen reactivity, which is directly related to the oxygen mobility and redox properties of the material. The OSC was calculated from the amount of O<sub>2</sub> consumed after an H<sub>2</sub> pulse, and this value corresponds to the most active and available oxygen species for reaction. The OSCC corresponds to the total amount of reactive oxygen species (surface plus bulk), and it was evaluated based on the total amount of oxygen consumed after a series of H<sub>2</sub> pulses until complete reaction of the materials. These analyses also provide information on the reoxidation capacity of the material using oxygen from the gas phase, which is a determining property to avoid the loss of the catalyst activity [45].

To determine the oxygen storage capacity of the catalysts in the temperature range used in VOC oxidation (100–400 °C), the OSC of the materials was evaluated under dynamic conditions at different temperatures. This study collected data on the more labile or reactive oxygen species that can participate in oxidation reactions as well as the redox ability of the materials, which stimulates the electron transfer in the VOC oxidation mechanism.

Figure 7 summarizes the OSC results under dynamic conditions at different temperatures for the Co-Mn mixed oxides synthesized by the two methodologies. It should be noted that the OSC obtained for the Mg-Al oxide obtained by auto-combustion does not indicate important oxygen consumption in the studied temperature range; thus, the redox behavior and OSC are attributed exclusively to the presence of Mn and Co in the oxides.

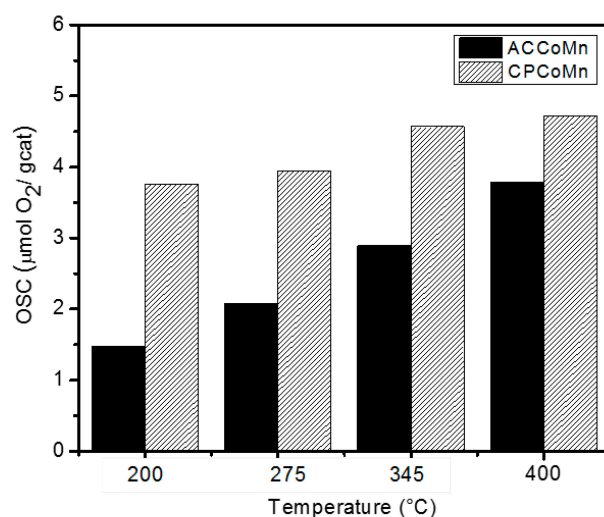


**Figure 7.** OSC of the mixed oxides at different temperatures.

The OSC increases with increases of temperature because of the participation of lattice oxygen that migrate and are available for the reaction [46]. At temperatures <300 °C, the oxygen at the surface and close to the surface contribute to the OSC, whereas at temperatures >300 °C, the migration of bulk oxygen plays an important role in the OSC performance [47].

The temperature dependence of the OSC is also verified in Table 2, where values for the mixed oxides are recorded after two H<sub>2</sub>-O<sub>2</sub> pulse cycles at different temperatures, which indicated that the

oxygen consumption was similar in the two cycles in both materials, suggesting reversibility in the redox process. These results show successful electron transfer by the Co and Mn mixed oxides because of the presence of phases such as  $\text{Mn}_3\text{O}_4$  and  $\text{Co}_3\text{O}_4$ , ( $\text{M}^{2+}$  and  $\text{M}^{3+}$ ), which present different oxidation states inside the structure and act as active components in the redox system.

**Table 2.** Oxygen storage capacity of the mixed oxides at different temperatures.

Sample	OSC ( $\mu\text{molO}_2/\text{g cat}$ ) two $\text{H}_2\text{-O}_2$ pulse cycles							
	200 °C		275 °C		345 °C		400 °C	
ACCoMn	1.6	1.5	2.1	1.9	3.0	2.9	3.9	3.7
CPCoMn	3.9	3.7	4.0	4.2	4.7	4.5	4.7	4.8

Figure 7 shows that the redox properties and oxygen mobility are superior in the oxide obtained by co-precipitation; this result is most likely because of the incorporation of Co into the Mn oxide structure, which increases the migration of lattice oxygen and generation of vacancies in the structure and leads to the formation of weak bonds with oxygen species and increased OSC. The OSCC can be used to study the total amount of oxygen species available in the oxides (surface plus bulk) that act as a reserve bank and contribute to the reoxidation of the catalyst, continuing the redox cycle even when gaseous oxygen is absent in the reaction current [12].

Figure 8 shows the OSCC of the Co-Mn mixed oxides at 400 °C along with that of the Mg-Al oxide obtained by auto-combustion. Although the ACCoMn and CPCoMn oxide present the same chemical composition, the oxygen storage capacity is affected by the synthesis method, with the oxide obtained by co-precipitation (CPCoMn) showing the most important OSCC value.

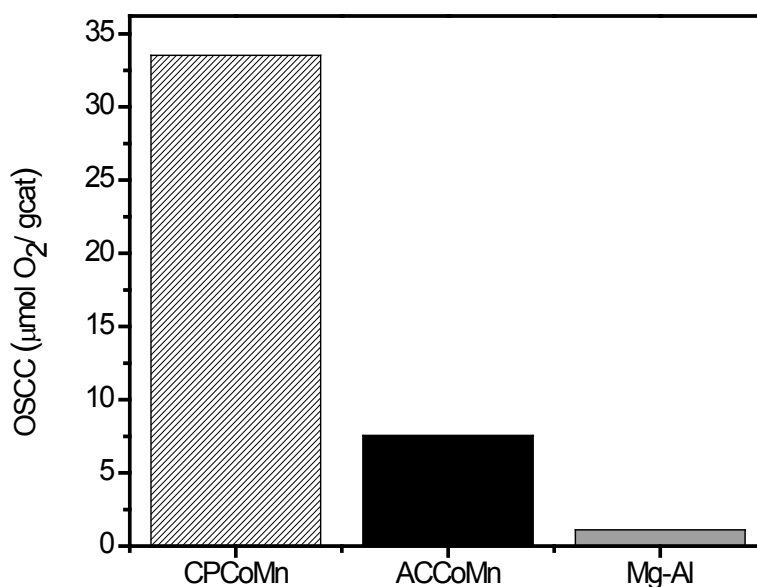


**Figure 8.** OSCC of the Co-Mn mixed oxides evaluated at 400 °C.

The maximum amount of both surface as well as lattice oxygen species that can participate in the catalytic oxidation of VOCs is determined at 400 °C, and the average OSC values of ACCoMn and CPCoMn are 3.8 and 4.8  $\mu\text{molO}_2/\text{g cat}$ ., respectively, whereas the OSCC at that temperature corresponds to 7.6 and 33.5  $\mu\text{molO}_2/\text{g cat}$ ., respectively. It is evident that there is a greater contribution of lattice

oxygen in the CPCoMn solid (~86%) compared with that of the ACCoMn oxide (~50%). However, the results show the joint participation of the surface and lattice oxygen in both materials during the oxidation reactions.

The H<sub>2</sub>-TPR, OSC and OSCC analyses revealed that the synthesis method influences the oxygen storage capacity, redox properties and oxygen species migration in the structure and demonstrated that the co-precipitation methodology promotes such properties. Although small crystallite sizes favor the formation of easily reducible species [48], crystallite size did not appear to determine the redox behavior of the evaluated materials because CPCoMn exhibits the most important values of OSC, OSCC and lowest reduction temperatures, but shows the largest particle size.

Considering that the materials with high specific areas show more active sites to adsorb O<sub>2</sub> from the gaseous phase and more active oxygen species [49], the study of the relation between the specific area and OSC was investigated by several authors [46,50,51]. Kamiuchi *et al.* [50] studied the OSC of Pt catalysts supported on Ce-Zr oxides calcined at 800 °C and 1000 °C whose areas correspond to 64 m<sup>2</sup>/g and 25 m<sup>2</sup>/g, respectively. However, the OSC values were comparable for materials with different areas (~400 μmol g<sup>-1</sup>), indicating that the OSC of the Pt/CZ catalysts is independent of the specific area. Likewise, Mamontov *et al.* [51] found a poor relation between the specific area and the OSC in Ce-Zr oxides while they established a direct correlation between the oxygen vacancies, the presence of defects and the OSC. On the other hand, in Ce-Co oxides, Wang *et al.* [47] suggested that the incorporation of Co in the structure of CeO<sub>2</sub> leads a lattice distortion with the generation of oxygen vacancies, which lead to a promotion of OSC in the Co-Ce oxides with respect to the individual Ce oxide.

Taking into account the aforementioned research, the OSC values determined in the present work are attributed mainly to the presence of vacancies by the incorporation of Co in the structure of the manganese oxide, being most important in the oxide obtained by co-precipitation CPCoMn as demonstrated by the TPR-H<sub>2</sub> y OSC results. Then, the specific area does not appear to be a determining factor in the OSC of the Co-Mn oxides evaluated in the present work.

The isotopic exchange technique is one of the most frequently used methods of evaluating oxygen mobility.

There are three pathways through which O<sup>18</sup>/O<sup>16</sup> exchange can be conducted [30,52,53]:

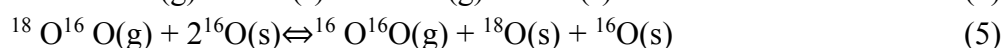
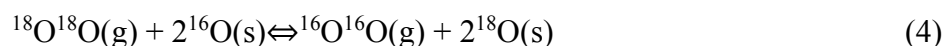
1. Homogeneous exchange: this reaction does not require the participation of oxygen atoms in the solid, and the concentrations of <sup>16</sup>O and <sup>18</sup>O remain constant during the test:



2. Heterogeneous single exchange: this reaction involves an oxygen atom from the oxide and an oxygen atom from the gas phase:



3. Heterogeneous multiple exchange: this reaction assumes the participation of two atoms of the solid in each step:



Isotopic exchange experiments with O<sup>18</sup>/O<sup>16</sup> were performed in a temperature range from 200 °C to 400 °C to evaluate oxygen mobility under reaction conditions (VOC oxidation). Figure 9 shows the

isotopic exchange of Co-Mn mixed oxides obtained by the two synthesis methodologies as well as Mg-Al oxide. In general, the exchange increases with temperature with exchange representing a decrease in the concentration of signal 36 ( $^{18}\text{O}_2$ ) and increase of the concentrations of signals 32 ( $^{16}\text{O}_2$ ) and 34 ( $^{18}\text{O}^{16}\text{O}$ ) in the reaction current. However, the isotopic exchange mainly occurs through the Mn and Co species because in the oxide consisting of Mg-Al, the concentrations of  $^{18}\text{O}_2$  and  $^{16}\text{O}_2$  species are approximately 85% and 14%, respectively, and a significant change does not occur with temperature. Furthermore, the maximum amount of  $^{18}\text{O}^{16}\text{O}$  occurs at 400 °C and corresponds to a concentration of approximately 3%.

Because the concentration of  $^{18}\text{O}^{16}\text{O}$  in the oxides is variable and depends on the nature of the solid, the gas phase reaction may be considered negligible (Equation 1). In addition, the difference in concentrations between signals 34 and 32 ( $^{18}\text{O}^{16}\text{O}$  and  $^{16}\text{O}_2$ ) suggests the presence of the two heterogeneous exchange mechanisms in the oxides: simple (Equations 2–3) and multiple (Equations 4–6).

By comparing the concentrations of  $^{18}\text{O}_2$ ,  $^{16}\text{O}_2$  and  $^{18}\text{O}^{16}\text{O}$  at 400 °C in the mixed oxides, a beneficial effect was observed in the oxygen mobility in the CPCoMn oxide related to increased concentrations of  $^{16}\text{O}_2$  (48%) and  $^{18}\text{O}^{16}\text{O}$  (15%) and decreased concentration of  $^{18}\text{O}_2$  (38%) concentration compared with that of ACCoMn ( $^{16}\text{O}_2$  (22%),  $^{18}\text{O}^{16}\text{O}$  (5%), and  $^{18}\text{O}_2$  (73%).

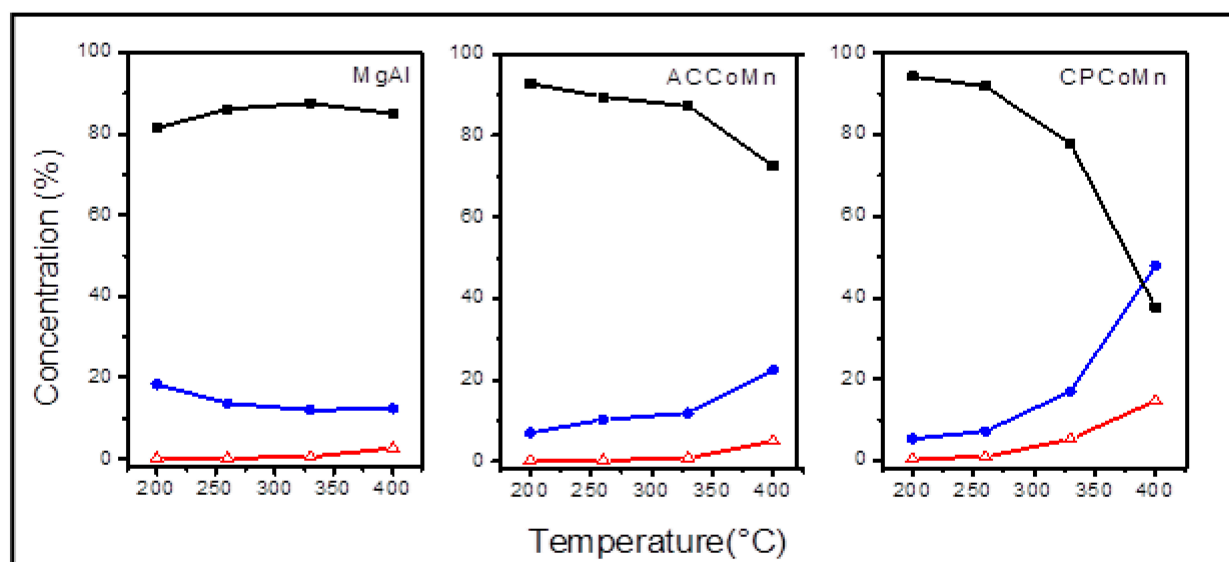


**Figure 9.** Isotopic exchange with the Co-Mn and Mg-Al mixed oxides. (■)  $^{18}\text{O}_2$  (36); (●)  $^{16}\text{O}_2$  (32); (Δ)  $^{18}\text{O}^{16}\text{O}$  (34).

In addition, isotopic exchange mainly occurs after 320 °C and 270 °C in ACCoMn and CPCoMn, respectively, indicating that in this last solid, the mobility of the lattice oxygen is high because oxygen is capable of participating in the exchange process even at temperatures <300 °C, which usually indicates the participation of surface oxygen species.

The isotopic exchange results confirm that the lattice oxygen from the Co-Mn oxides synthesized by both methodologies participates in the oxidation reactions, and their participation is more important in the CPCoMn solid. These results are consistent with the analysis performed based on the H<sub>2</sub>-TPR, OSC and OSCC results.

### 2.2.3. Oxidation Reaction

VOCs from mobile and stationary sources of emission are present as mixtures and not individually, which has increased interest in the evaluation of the oxidation of VOC mixtures. Figure 9 shows the conversion of mixtures of two VOCs (toluene and 2-propanol) towards CO<sub>2</sub> in the studied oxides. The oxidation of toluene and 2-propanol mixture is not 100% selective towards CO<sub>2</sub> because acetone and propene appear as intermediate products of the reaction. These results are consistent with those reported for the individual oxidation of 2-propanol, where ketone and alkene are formed from the dehydrogenation and dehydration reactions of the alcohol [54].

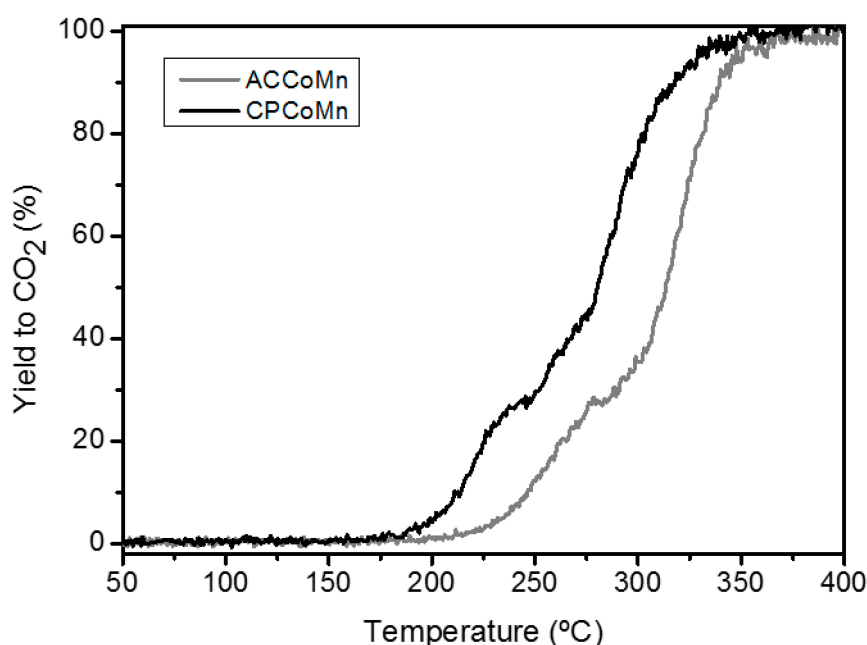


**Figure 10.** Catalytic performance of the mixed oxides in the oxidation of the VOC mixture.

The  $T_{50}$  and  $T_{90}$  values that correspond to the temperatures required to reach 50 and 90% conversions towards CO<sub>2</sub>, respectively, are used to compare the catalytic performance of the oxides. Table 3 presents the  $T_{50}$  and  $T_{90}$  values of the ACCoMn and CPCoMn oxides, where lower conversion temperatures are observed with the solid synthesized by co-precipitation, which implies a better catalytic performance in the oxidation of the VOC mixture. Furthermore, the conversion temperatures are related to the OSC and the exchange capacity in terms of the <sup>16</sup>O<sub>2</sub> concentration, which indicates that the catalytic properties of the materials are directly dependent on their redox properties and oxygen mobility. Thus, CPCoMn shows greater OSC values at the respective  $T_{90}$  and  $T_{50}$  because of the greater concentrations of <sup>16</sup>O<sub>2</sub>. In addition, CPCoMn exhibits the greatest catalytic activity towards the total combustion of the VOC mixture (Figure 10), with complete conversion towards CO<sub>2</sub> and H<sub>2</sub>O occurring at 360 °C, which is lower than the temperature required for ACCoMn to achieve total oxidation (370 °C). The relation between oxygen mobility and catalytic behavior is likewise reported by Cimino *et al.* [55] regarding hexaaluminates of Mn and La synthesized by auto-combustion and co-precipitation, where the catalysts prepared by co-precipitation showed better oxygen mobility and therefore a better catalytic behavior in the combustion of methanol.

Based on the information provided by the OSC values on the most labile oxygen species and isotopic exchange analysis on the lattice oxygen, the correlation results demonstrate the joint participation of surface and lattice oxygen in the oxidation of the VOC mixture on the mixed oxides.

Additionally, in Table 3 the catalytic behavior of the Co-Mn oxides is compared with that of the reference 1%Pt/Al<sub>2</sub>O<sub>3</sub> [9] where it is shown that the mixed oxides present higher conversion temperatures to the latter. The reason for this behavior is that the total oxidation of VOCs is determined by the compound that is the most difficult to oxidize which in this case is toluene—a compound easily oxidized by the Pt/Al<sub>2</sub>O<sub>3</sub> that is the most active metal for the conversion of aromatic structures [56].

**Table 3.** Temperatures of conversion of the VOC mixture and their relationship with the OSC and isotopic exchange.

Sample	Yield to CO <sub>2</sub> temperatures (°C)		OSC (μmolO <sub>2</sub> / g cat.)*		<sup>16</sup> O <sub>2</sub> concentration (%) *	
	T <sub>90</sub>	T <sub>50</sub>	T <sub>90</sub>	T <sub>50</sub>	T <sub>90</sub>	T <sub>50</sub>
ACCoMn	340	312	2.9	2.4	12	10
CPCoMn	320	280	4.4	4.1	14	8
1%Pt/Al <sub>2</sub> O <sub>3</sub>	195	180	-	-	-	-

\* The values are calculated at the respective temperatures to reach 50% and 90% conversion of the VOC mixture.

### 3. Experimental Section

#### 3.1. Synthesis of Catalysts

##### 3.1.1. Auto-Combustion

For the synthesis of the Co-Mn-Mg-Al mixed oxide by the auto-combustion method, solutions of Mg(NO<sub>3</sub>)<sub>2</sub>·6H<sub>2</sub>O, Al(NO<sub>3</sub>)<sub>3</sub>·9H<sub>2</sub>O, Mn(NO<sub>3</sub>)<sub>2</sub>·6H<sub>2</sub>O and/or Co(NO<sub>3</sub>)<sub>2</sub>·6H<sub>2</sub>O nitrates were used as oxidizers, and a solution of glycine [CH<sub>2</sub>NH<sub>2</sub>COOH] was used as fuel, maintaining constant molar ratios of [(Mg<sup>2+</sup> + Mn<sup>2+</sup> + Co<sup>2+</sup>) / Al<sup>3+</sup> = 3], [(Mn<sup>2+</sup> + Co<sup>2+</sup>) / Mg<sup>2+</sup> = 1] and [Co<sup>2+</sup> / Mn<sup>2+</sup> = 0.5] and a fuel/oxidizer ratio of 0.56.

The ACCoMn mixed oxide was produced by the addition of the respective nitrates to glycine, maintaining constant agitation. The resulting solution was slowly evaporated until a gel was obtained, and it was heated at approximately 100 °C to initiate the ignition process (~10 min). Once the ignition reaction is completed (~3 min), a powder is produced, and it is then calcined at 500 °C for 4 h to remove the remaining carbonaceous residues and obtain the corresponding oxide.

### 3.1.2. Co-Precipitation

The CPCoMn mixed oxide was synthesized by thermal decomposition of the hydrotalcite-type precursor (HTCoMn) obtained by the simultaneous co-precipitation method, which used solutions of the respective nitrates. The molar ratios used in the mixed oxide synthesized by auto-combustion were maintained.

The mixture  $Mg^{2+}$ ,  $Al^{3+}$ ,  $Mn^{2+}$  and/or  $Co^{2+}$  nitrates was added drop by drop to a 0.2 M  $K_2CO_3$  solution under constant agitation, with the pH maintained at 9.5 and 10.5 by addition of a 1 M NaOH solution. The obtained precipitate was aged for 18 h without agitation. Subsequently, the solid was washed and dried at 60 °C in air for 18 h to obtain the hydrotalcite and calcined at 500 °C for 16 h to obtain the respective mixed oxide.

### 3.2. Characterization

The chemical analysis of the materials was performed using an X-ray fluorescence spectrometer MagixPro PW-2440 (Phillips), which has a maximum power of 4 KW.

The composition of the phases present in the oxides was determined by the XRD in a Panalytical X'Pert PRO MPD instrument equipped with a copper anode ( $\lambda = 1.5406 \text{ \AA}$ ), using a scan speed of  $1^\circ \theta \text{ min}^{-1}$  and step size of  $0.02^\circ \theta$ . The particle size was calculated with the Scherrer equation using the most intense signal corresponding to each oxide.

The Raman spectra were collected in a dispersion spectrometer (Horiva Jobin Yvon LabRam HR800) with a He-Ne green laser at 20 mW (532.1 nm) without a filter and with a  $600 \text{ g mm}^{-1}$  grid. The microscope uses an objective of 50 with a confocal aperture of  $1000 \text{ \mu m}$  [45].

The scanning electron micrographs (SEM) were collected using a Hitachi S2700 equipped with an energy-dispersive X-ray spectrometer (Bruker Quantax 400).

The  $H_2$ -TPR was performed in a ChemBET 3000 Quantachrome equipped with a thermal conductivity detector. The materials (0.100 g) were previously degassed at 400 °C for 1 h in the presence of Ar and reduced using a 10% (v/v)  $H_2/Ar$  mixture at a flow rate of 30 mL/min and a heating ramp of 10 °C/min. The hydrogen consumption was calculated from a CuO calibration curve, and OriginPro 8.0 software was used to quantify the areas associated with the  $H_2$  consumption.

The OSC and  $^{18}O/^{16}O$  isotopic exchange analyses were performed in a device designed and tuned by a group at Estado Sólido y Catálisis Ambiental (ESCA). For the OSC analyses, two measurements were performed: (i) OSC, and (ii) OSC under dynamic conditions.

Prior to performing the two measurements, the samples (0.015 g in 0.100 g of SiC) were pre-oxidized under an air flow of 10 mL/min (21%  $O_2$ ) at 400 °C for 40 min and subsequently purged with Ar until the  $^{16}O_2$  was not detected.

In the OSC measurements, after the pretreatment, the samples were cooled to 200 °C under Ar flow (10 mL/min) and alternating pulses of  $H_2-O_2$  at 50  $\mu L$  were performed until two cycles were completed. To determine the amount of available oxygen in the solids within a temperature range, this same procedure was used at temperatures of approximately 275, 345 and 400 °C.

The concentration of the output gases  $H_2$ ,  $O_2$ ,  $H_2O$ , Ar, and He were monitored by mass spectroscopy (Omnistar mass spectrometer) at  $m/z = 2, 32, 18, 40$  and 4, respectively.

For the OSCC analysis, the temperature was kept constant at 400 °C, Ar flow was maintained at 10 mL/min, successive H<sub>2</sub> (99.99%) pulses of 50 µL were injected until saturation of the samples, and two successive O<sub>2</sub> pulses (15.2% in He) of 50 µL were injected to reoxidize the solid until O<sub>2</sub> consumption was not observed.

The OSCC and OSC were calculated based on the amount of oxygen consumed during the reoxidation stage after the H<sub>2</sub> pulses, and the values were expressed in terms of µmolO<sub>2</sub> g<sup>-1</sup> of catalyst. OriginPro 8.0 software was used to quantify the areas of each pulse associated with the O<sub>2</sub> signal.

For the isotopic exchange tests, the samples (0.030 g with 0.100 g of SiC) were treated under an air current (10 mL/min) at 400 °C for 1 h. After the pretreatment, the sample was left to cool down to 200 °C under Ar flow. Pulses of <sup>18</sup>O<sub>2</sub> (20 µL) were performed on the samples at 200, 260, 330 and 400 °C in the presence of an Ar current (10 mL/min). The output gas composition was monitored by mass spectroscopy (Omnistar mass spectrometer) at *m/z* = 36, 34 and 32, which corresponded to <sup>18</sup>O<sub>2</sub>, <sup>18</sup>O <sup>16</sup>O and <sup>16</sup>O<sub>2</sub>, respectively. OriginPro 8.0 software was used to quantify the areas under the signals associated with the concentration of each of the species.

### 3.3. Catalytic Evaluation

To evaluate the catalytic performance of the Co-Mn mixed oxides obtained by the auto-combustion and co-precipitation methodologies, a mixture of 250 ppm toluene and 250 ppm 2-propanol in air was employed.

The catalysts were pretreated in air at 400 °C for 1 h before starting the reaction. The complete oxidation of the VOCs was conducted in a fixed-bed tubular reactor at atmospheric pressure with a heating ramp of 1.5 °C/min. The VOC liquid mixture was fed with a high-performance liquid chromatography (HPLC) pump (Jasco PU 1585) and diluted with air until the desired composition was obtained. A total flow of 500 mL/min and 0.200 g catalyst (sieved at <250 µm) were used. The reaction products were detected with a mass spectrometer (Balzers Instruments, Omnistar) and CO<sub>2</sub> detector (Sensotrans IR). The performance towards CO<sub>2</sub> was calculated as the ratio between the CO<sub>2</sub> concentration at any temperature divided by its value when complete conversion is reached at high temperatures and no other oxidation products are observed.

## 4. Conclusions

Co-Mn-Mg-Al oxides were successfully obtained by the auto-combustion and co-precipitation methodologies. The formation of a hydrotalcite-type precursor was verified in the production of the CPCoMn oxide, whereas the mixed oxide is directly generated through the synthesis by auto-combustion.

A Co-Mn mixed oxide with greater crystallite size was obtained through co-precipitation. However, a cooperative effect may occur between Co and Mn that increases the redox properties and oxygen mobility and improves the catalytic activity, demonstrating that crystal size is not a determinant in the catalytic performance of the material. The catalytic behavior in the total oxidation of the binary mixture of toluene and 2-propanol is dependent on the redox properties of the solid; thus, the catalyst that presents greater OSC values exhibits the lowest conversion temperatures.

## Acknowledgments

The authors would like to thank Professor Mario Montes of the Universidad del País Vasco (Spain), for his support during the catalytic tests and the Instituto de Ciencia de Materiales de Sevilla (ICMS), from the Universidad de Sevilla for conducting the Raman and SEM analyses of the solids studied in the present work.

## Author Contributions

M. Haidy Castaño carried out the experimental work and analyzed the data; Rafael Molina and Sonia Moreno supervised all of the study.

## Conflicts of Interest

The authors declare no conflict of interest

## References

1. Bastos, S.S.T.; Carabineiro, S.A.C.; Órfão, J.J.M.; Pereira, M.F.R.; Delgado, J.J.; Figueiredo, J.L. Total oxidation of ethyl acetate, ethanol and toluene catalyzed by exotemplated manganese and cerium oxides loaded with gold. *Catal. Today* **2012**, *180*, 148–154.
2. Domínguez, M.I.; Sánchez, M.; Centeno, M.A.; Montes, M.; Odriozola, J.A. 2-Propanol oxidation over gold supported catalysts coated ceramic foams prepared from stainless steel wastes. *J. Mol. Catal. A* **2007**, *277*, 145–154.
3. Liu, S.Y.; Yang, S.M. Complete oxidation of 2-propanol over gold-based catalysts supported on metal oxides. *Appl. Catal. A* **2008**, *334*, 92–99.
4. Aguilera, D.A.; Perez, A.; Molina, R.; Moreno, S. Cu–Mn and Co–Mn catalysts synthesized from hydrotalcites and their use in the oxidation of VOCs. *Appl. Catal. B* **2011**, *104*, 144–150.
5. Tsou, J.; Magnoux, P.; Guisnet, M.; Órfão, J.J.M.; Figueiredo, J.L. Catalytic oxidation of volatile organic compounds: Oxidation of methyl-isobutyl-ketone over Pt/zeolite catalysts. *Appl. Catal. B* **2005**, *57*, 117–123.
6. He, C.; Li, P.; Cheng, J.; Hao, Z.-P.; Xu, Z.-P. A Comprehensive Study of Deep Catalytic Oxidation of Benzene, Toluene, Ethyl Acetate; their Mixtures over Pd/ZSM-5 Catalyst: Mutual Effects and Kinetics. *Water Air Soil Pollut.* **2010**, *209*, 365–376.
7. Burgos, N.; Paulis, M.a.; Mirari Antxustegi, M.; Montes, M. Deep oxidation of VOC mixtures with platinum supported on Al<sub>2</sub>O<sub>3</sub>/Al monoliths. *Appl. Catal. B* **2002**, *38*, 251–258.
8. Beauchet, R.; Mijoin, J.; Batonneau-Gener, I.; Magnoux, P. Catalytic oxidation of VOCs on NaX zeolite: Mixture effect with isopropanol and o-xylene. *Appl. Catal. B* **2010**, *100*, 91–96.
9. Sanz, O.; Delgado, J.J.; Navarro, P.; Arzamendi, G.; Gandía, L.M.; Montes, M. VOCs combustion catalysed by platinum supported on manganese octahedral molecular sieves. *Appl. Catal. B* **2011**, *110*, 231–237.
10. Fierro, J.L.G. Applications of Metal Oxides for Volatile Organic Compound Combustion. *Metal Oxides, Chemistry and Applications*; CRC Press: New York, NY, USA, 2006; pp. 543–555.

11. Liotta, L.F.; Wu, H.; Pantaleo, G.; Venezia, A.M. Co<sub>3</sub>O<sub>4</sub> nanocrystals and Co<sub>3</sub>O<sub>4</sub>-MO<sub>x</sub> binary oxides for CO, CH<sub>4</sub> and VOC oxidation at low temperatures: A review. *Catal. Sci. Tech.* **2013**, *3*, 3085–3102.
12. Santos, V.P.; Pereira, M.F.R.; Órfão, J.J.M.; Figueiredo, J.L. The role of lattice oxygen on the activity of manganese oxides towards the oxidation of volatile organic compounds. *Appl. Catal. B* **2010**, *99*, 353–363.
13. Liotta, L.F.; Ousmane, M.; di Carlo, G.; Pantaleo, G.; Deganello, G.; Marci, G.; Retailleau, L.; Giroir-Fendler, A. Total oxidation of propene at low temperature over Co<sub>3</sub>O<sub>4</sub>-CeO<sub>2</sub> mixed oxides: Role of surface oxygen vacancies and bulk oxygen mobility in the catalytic activity. *Appl. Catal. A* **2008**, *347*, 81–88.
14. Zhu, L.; Lu, G.; Wang, Y.; Guo, Y.; Guo, Y. Effects of Preparation Methods on the Catalytic Performance of LaMn<sub>0.8</sub>Mg<sub>0.2</sub>O<sub>3</sub> Perovskite for Methane Combustion. *Chin. J. Catal.* **2010**, *31*, 1006–1012.
15. Avgouropoulos, G.; Ioannides, T.; Matralis, H. Influence of the preparation method on the performance of CuO-CeO<sub>2</sub> catalysts for the selective oxidation of CO. *Appl. Catal. B* **2005**, *56*, 87–93.
16. Kovanda, F.; Jirátová, K. Supported layered double hydroxide-related mixed oxides and their application in the total oxidation of volatile organic compounds. *Appl. Clay. Sci.* **2011**, *53*, 305–316.
17. Vaccari, A. Preparation and catalytic properties of cationic and anionic clays. *Catal. Today* **1998**, *41*, 53–71.
18. Cavani, F.; Trifirò, F.; Vaccari, A. Hydrotalcite-type anionic clays: Preparation, properties and applications. *Catal. Today* **1991**, *11*, 173–301.
19. Mukasyan, A.; Dinka, P. Novel approaches to solution-combustion synthesis of nanomaterials. *Int. J. Self-Propag. High-Temp Synth.* **2007**, *16*, 23–35.
20. Tahmasebi, K.; Paydar, M.H. The effect of starch addition on solution combustion synthesis of Al<sub>2</sub>O<sub>3</sub>-ZrO<sub>2</sub> nanocomposite powder using urea as fuel. *Mater. Chem. Phys* **2008**, *109*, 156–163.
21. Castaño, M.H.; Molina, R.; Moreno, S. Catalytic oxidation of VOCs on MnMgAlO<sub>x</sub> mixed oxides obtained by auto-combustion. *J. Mol. Catal. A* **2015**, *398*, 358–367.
22. Tsyganok, A. and Sayari, A. Incorporation of transition metals into Mg–Al layered double hydroxides: Coprecipitation of cations vs. their pre-complexation with an anionic chelator. *J. Solid State Chem.* **2006**, *179*, 1830–1841.
23. Xu, Z.P.; Zhang, J.; Adebajo, M.O.; Zhang, H.; Zhou, C. Catalytic applications of layered double hydroxides and derivatives. *Appl. Clay. Sci.* **2011**, *53*, 139–150.
24. Lamonier, J.-F.; Boutoundou, A.-B.; Gennequin, C.; Pérez-Zurita, M.; Siffert, S.; Aboukais, A. Catalytic Removal of Toluene in Air over Co–Mn–Al Nano-oxides Synthesized by Hydrotalcite Route. *Catal. Lett.* **2007**, *118*, 165–172.
25. Evans, D.G. and Duan, X.; *Structural Aspects of Layered Double Hydroxides*, in *Structure and Bonding*; Springer-Verlag: Berlin & Heidelberg: Germany, 2006; p. 15.
26. Tsai, Y.-T.; Mo, X.; Campos, A.; Goodwin, J.G., Jr.; Spivey, J.J. Hydrotalcite supported Co catalysts for CO hydrogenation. *Appl. Catal. A* **2011**, *396*, 91–100.

27. Hem John, D.; Redox Coprecipitation Mechanisms of Manganese Oxides. In *Particulates in Water*; American Chemical Society: Menlo Park, CA, USA, 1980; pp. 45–72.
28. Sinha, A.P.B.; Sanjana, N.R.; Biswas, A.B. On the structure of some manganites. *Acta Crystallogr.* **1957**, *10*, 439–440.
29. Leofanti, G.; Padovan, M.; Tozzola, G.; Venturelli, B. Surface area and pore texture of catalysts. *Catal. Today* **1998**, *41*, 207–219.
30. Castaño, M.H.; Molina, R.; Moreno, S. Cooperative effect of the Co–Mn mixed oxides for the catalytic oxidation of VOCs: Influence of the synthesis method. *Appl. Catal. A* **2015**, *492*, 48–59.
31. Julien, C.M.; Massot, M.; Poinsignon, C. Lattice vibrations of manganese oxides: Part I. Periodic structures. *Spectrochim. Acta Part A* **2004**, *60*, 689–700.
32. Jiang, J. and Li, L. Synthesis of sphere-like Co<sub>3</sub>O<sub>4</sub> nanocrystals via a simple polyol route. *Mater. Lett.* **2007**, *61*, 4894–4896.
33. Ulla, M.A.; Spretz, R.; Lombardo, E.; Daniell, W.; Knözinger, H. Catalytic combustion of methane on Co/MgO: Characterisation of active cobalt sites. *Appl. Catal. B* **2001**, *29*, 217–229.
34. Rezaei, E. and Soltan, J. Low temperature oxidation of toluene by ozone over MnO<sub>x</sub>/γ-alumina and MnO<sub>x</sub>/MCM-41 catalysts. *Chem. Eng. J.* **2012**, *198–199*, 482–490.
35. Mars, P. and van Krevelen, D.W. Oxidations carried out by means of vanadium oxide catalysts. *Chem. Eng. Sci.* **1954**, *3*, 41–59.
36. Fierro, J.L.G. *Metal Oxides, Chemistry and Applications*; CRC Press: New York, NY, USA, 2006.
37. Ran, R.; Weng, D.; Wu, X.; Fan, J.; Wang, L.; Wu, X. Structure and oxygen storage capacity of Pr-doped Ce<sub>0.26</sub>Zr<sub>0.74</sub>O<sub>2</sub> mixed oxides. *J. Rare Earth* **2011**, *29*, 1053–1059.
38. Muñoz, M.; Moreno, S.; Molina, R. Promoting effect of Ce and Pr in Co catalysts for hydrogen production via oxidative steam reforming of ethanol. *Catal. Today* **2013**, *213*, 33–41.
39. Coq, B.; Tichit, D.; Ribet, S. Co/Ni/Mg/Al Layered Double Hydroxides as Precursors of Catalysts for the Hydrogenation of Nitriles: Hydrogenation of Acetonitrile. *J. Catal.* **2000**, *189*, 117–128.
40. Pérez, A.; Lamonier, J.-F.; Giraudon, J.-M.; Molina, R.; Moreno, S. Catalytic activity of Co-Mg mixed oxides in the VOC oxidation: Effects of ultrasonic assisted in the synthesis. *Catal. Today* **2011**, *176*, 286–291.
41. Döbber, D.; Kießling, D.; Schmitz, W.; Wendt, G. MnO<sub>x</sub>/ZrO<sub>2</sub> catalysts for the total oxidation of methane and chloromethane. *Appl. Catal. B* **2004**, *52*, 135–143.
42. Stobbe, E.R.; de Boer, B.A.; Geus, J.W. The reduction and oxidation behaviour of manganese oxides. *Catal. Today* **1999**, *47*, 161–167.
43. Li, Q.; Meng, M.; Xian, H.; Tsubaki, N.; Li, X.; Xie, Y.; Hu, T.; Zhang, J. Hydrotalcite-Derived Mn<sub>x</sub>Mg<sub>3-x</sub>AlO Catalysts Used for Soot Combustion, NO<sub>x</sub> Storage and Simultaneous Soot-NO<sub>x</sub> Removal. *Environ. Sci. Technol.* **2010**, *44*, 4747–4752.
44. Hwang, C.-C.; Wu, T.-Y.; Wan, J.; Tsai, J.-S. Development of a novel combustion synthesis method for synthesizing of ceramic oxide powders. *Mater. Sci. Eng. B* **2004**, *111*, 49–56.
45. Gonzalez Castaño, M.; Reina, T.R.; Ivanova, S.; Centeno, M.A.; Odriozola, J.A. Pt vs. Au in water–gas shift reaction. *J. Catal.* **2014**, *314*, 1–9.
46. Zhao, M.; Shen, M.; Wang, J. Effect of surface area and bulk structure on oxygen storage capacity of Ce<sub>0.67</sub>Zr<sub>0.33</sub>O<sub>2</sub>. *J. Catal.* **2007**, *248*, 258–267.

47. Wang, J.; Shen, M.; Wang, J.; Gao, J.; Ma, J.; Liu, S. CeO<sub>2</sub>–CoO<sub>x</sub> mixed oxides: Structural characteristics and dynamic storage/release capacity. *Catal. Today* **2011**, *175*, 65–71.
48. de Rivas, B.; López-Fonseca, R.; Jiménez-González, C.; Gutiérrez-Ortiz, J.I. Synthesis, characterisation and catalytic performance of nanocrystalline Co<sub>3</sub>O<sub>4</sub> for gas-phase chlorinated VOC abatement. *J. Catal.* **2011**, *281*, 88–97.
49. Cui, M.; Li, Y.; Wang, X.; Wang, J.; Shen, M. Effect of preparation method on MnO<sub>x</sub>-CeO<sub>2</sub> catalysts for NO oxidation. *J. Rare Earth* **2013**, *31*, 572–576.
50. Kamiuchi, N.; Haneda, M.; Ozawa, M. Enhancement of OSC property of Zr rich ceria–zirconia by loading a small amount of platinum. *Catal. Today* **2014**, *232*, 179–184.
51. Mamontov, E.; Egami, T.; Brezny, R.; Koranne, M.; Tyagi, S. Lattice Defects and Oxygen Storage Capacity of Nanocrystalline Ceria and Ceria-Zirconia. *J. Phys. Chem. B* **2000**, *104*, 11110–11116.
52. Nováková, J. Isotopic exchange of oxygen <sup>18</sup>O between the gaseous phase and oxide catalysts. *Catal. Rev.* **1971**, *4*, 77–113.
53. Royer, S.; Duprez, D.; Kaliaguine, S. Role of bulk and grain boundary oxygen mobility in the catalytic oxidation activity of LaCo<sub>1-x</sub>Fe<sub>x</sub>O<sub>3</sub>. *J. Catal.* **2005**, *234*, 364–375.
54. Díez, V.K.; Apesteguía, C.R.; Di Cosimo, J.I. Acid–base properties and active site requirements for elimination reactions on alkali-promoted MgO catalysts. *Catal. Today* **2000**, *63*, 53–62.
55. Cimino, S.; Nigro, R.; Weidmann, U.; Holzner, R. Catalytic combustion of methanol over La, Mn-hexaaluminate catalysts. *Fuel Process. Technol.* **2015**, *133*, 1–7.
56. Golodets, G.I.; *Heterogeneous Catalytic Reactions Involving Molecular Oxygen*; Elsevier: Amsterdam, The Netherlands, 1983.

© 2015 by the authors; licensee MDPI, Basel, Switzerland. This article is an open access article distributed under the terms and conditions of the Creative Commons Attribution license (<http://creativecommons.org/licenses/by/4.0/>).